ChemPhotoChem

Research Articles
doi.org/10.1002/cptc.202200142

Chemistry Europe
European Chemical Societies Publishing

www.chemphotochem.org

Special Collection

Revisiting Ligand-to-Ligand Charge Transfer Phosphorescence Emission from Zinc(II) Diimine Bis-Thiolate Complexes: It is Actually Thermally Activated Delayed Fluorescence

Nora Lüdtke,[a] Julia Kuhnt,[b] Tabea Heil,[b] Andreas Steffen,*[b] and Christel M. Marian*[a]

In this work we revisit and re-evaluate the photophysical behavior of the prototypical complex [Zn(SC_6H_4-4-R)$_2$(phen)] as the most in-depth studied type of Zn(II)-based triplet state emitters. Previous reports suggest population of ligand-to-ligand charge transfer (LLCT) states via phenanthroline localized ππ* states, with an energy barrier between the ^{3}ππ* and the bk;$^{1/3}$LLCT states requiring thermal activation. Besides very weak prompt fluorescence, the dominant radiative mechanism was attributed to phosphorescence. Our photophysical studies, including temperature-dependent quantum yield determination and time-resolved luminescence measurements, reveal a high radiative rate constant $k_r = 3.5 \times 10^5\ s^{-1}$ at room temperature and suggest thermally activated luminescence as the major emission path. High-level DFT/MRCI calculations confirm this assignment and provide deeper insight into the excited-state kinetics, including rate constants for the (reverse) intersystem crossing processes. Thus, our study demonstrates that further optimization of the photophysical properties of this type of Zn(II) triplet exciton emitter bears great potential for future application in devices.

Introduction

Luminescent transition metal complexes play a vital role for the development of imaging agents, sensing applications, photocatalysts or as emitters in light generating devices. The latter application in particular depends on the efficiency of the luminophores to emit from triplet excited states because the excitation process leading to electroluminescence occurs via recombination of holes and electrons as charge carriers, generating 25% singlet and 75% triplet states according to spin statistics. Various strategies have been tested to harvest all excitons in electroluminescent devices, of which the two most promising appear to be the employment of phosphorescent transition metal complexes of 5d elements with high spin-orbit coupling (SOC) such as iridium or platinum, or of thermally activated delayed fluorescence (TADF) emitters.[1–3] Bypassing the spin-forbidden triplet emission via reverse intersystem-crossing (rISC) and subsequent spin-allowed luminescence from the S_1 state reduces the importance of SOC for triplet exciton harvesting, and even organic TADF emitters can be very attractive luminophores exhibiting high quantum yields and relatively short lifetimes of a few microseconds. It is noteworthy that a class of linearly coordinated photoactive d^{10} coinage metal complexes, designed according to a donor-acceptor motif, show particularly large radiative rate constants which can exceed $k_r > 2 \times 10^6\ s^{-1}$.[4–7] A small admixture of metal-to-ligand charge transfer (MLCT) character to the S_1 and T_1 states of dominantly ligand-to-ligand (LL)CT nature in those Cu^I/Ag^I/Au^I carbene amide complexes enhances the SOC contribution and accelerates the spin-forbidden processes.[8–10]

In contrast to group 11 metal complexes in their d^{10} electron configuration, light-emitting Zn(II) complexes are often brightly fluorescent with the lowest-lying states originating either from ligand-centered (LC) or LLCT excitations.[11–16] Owing to the high ionization potential of the Zn^{2+} core, MLCT contributions mediating SOC are not to be expected, although there are indications that ligand-to-metal (LM)CT excitations involving the 4p shell of Zn might contribute to the wave-functions of some complexes and thereby could enhance intersystem crossing (ISC). Consequently, electroluminescent Zn(II) complexes have mainly been employed as emitters in fluorescent OLEDs and as host materials for phosphorescent OLEDs containing iridium complexes as dopants.[17] However, Adachi and coworkers recently reported the use of a Zn(II) complex featuring $^{1/3}$intra-ligand ($^{1/3}$IL)CT states with very small singlet-triplet energy gap $\Delta E(T_1–S_1)$ for TADF-based OLEDs.[18] Mixed LLCT and ILCT transitions were also held responsible for the intense orange to deep red luminescence of triarylamine-

[a] N. Lüdtke, Prof. Dr. C. M. Marian
Institute of Theoretical and Computational Chemistry
Heinrich-Heine-University Düsseldorf
40204 Düsseldorf (Germany)
E-mail: Christel.Marian@hhu.de
[b] J. Kuhnt, T. Heil, Prof. Dr. A. Steffen
Faculty of Chemistry and Chemical Biology
TU Dortmund University,
Otto-Hahn-Str. 6, 44227 Dortmund (Germany)
E-mail: Andreas.Steffen@tu-dortmund.de

Supporting information for this article is available on the WWW under https://doi.org/10.1002/cptc.202200142

An invited contribution to a Special Collection on Emissive Materials for Organic Light Emitting Diodes

containing Zn(II) diimine bis-thiolate complexes, of which the authors do not define the type of emission, but we note that the quantum yield ϕ and observed lifetimes τ are indicative of fluorescence.[19]

Only a few phosphorescent Zn(II) complexes have been reported in the literature, including a hemicage Zn bipyridyl complex ZnL_3 (L_3 = *m*-(bpy(C_2H_4))$_3C_6H_3(CH_3)_3$, with bpy = 2,2′-bipyridine),[20] Zn porphyrins[21–23] and several representatives of a broader class of [Zn(thiolate)$_2$(diimine)] complexes.[24–30] Very recently, ultra-long lifetimes in the millisecond regime were reported for cyclic (alkyl)(amino)carbene (cAAC) complexes of Zn(II) halides at 77 K and shown to stem from ligand-centered triplet states.[31] While ISC and phosphorescence of Zn(II) porphyrins are known to be vibronically induced,[32] the underlying mechanisms operative in the Zn(II) diimine dithiolates are not well understood despite some very sophisticated and detailed studies conducted by Crosby and coworkers.[25,27,28] The authors observed for a series of [Zn(SC_6H_4-4-R)$_2$(phen)] complexes (phen = 1,10-phenanthroline; R=H, Cl, Me, OMe) temperature-dependent dual luminescence in organic glass and in the crystalline solid state that has been attributed to vibrationally resolved high energy phosphorescence from a ^{3}LC(phen) state with ultralong lifetimes in the millisecond regime and simultaneous broad emission from a lower energy LLCT state. Thermally modulated emission spectroscopy (TME) measurements suggest that these two luminescent states are not in thermal equilibrium and the following scheme has been proposed. Photoexcitation primarily populates high energy ^{1}LLCT and LC(phen) states, which convert via branched decay paths to vibrationally relaxed ^{1}LLCT, ^{3}LLCT, and ^{3}LC (phen) states (Scheme 1). Whether the ^{3}LLCT state is populated directly by vibrationally hot ^{1}LLCT and LC(phen) states or via the equilibrated ^{1}LLCT state remained an open question. Clear is that a path with a thermally surmountable barrier connects the energetically higher ^{3}LC(phen) minimum with the global minima of the S_1 and T_1 potentials, respectively, of LLCT type. A back transfer from the equilibrated LLCT states to the ^{3}LC (phen) state is not expected.

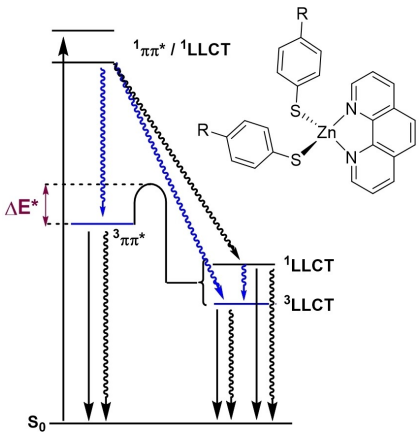

Scheme 1. Chemical structure of [Zn(SC_6H_4-4-R)$_2$(phen)] (R=H, Me, Cl, OMe) and excited-state decay mechanism upon photoexcitation as proposed by Crosby *et al.*[27,28]

Later work by Burt *et al.*[33] indicated that the barrier heights and transition probabilities might not only depend on the chemical composition of the Zn(II) complex. Specifically, luminescence studies at 5 K on structurally related [Zn(SC_6H_4-4-Cl)$_2$(2,9-Me$_2$-phen)] in the single crystalline solid state showed for the $P2_1/N$ phase a highly structured emission with λ_{max} at 452 nm and a broad, structureless emission with λ_{max} = 540 nm. The same general features are also found in PMMA films, but in the $P2_1/C$ crystal phase the complex exhibits only a structureless band at 570 nm. The high-energy band has been assigned to phosphorescence from a $^3\pi\pi^*$ state localized at the phen ligand, and the broader lower-energy band to LLCT transitions.[33] The authors conclude that the barrier is molecular in nature, but its height depends on the geometry determined by the packing in the crystals, which supports the original assumption by Highland *et al.*[27,28]

In conjunction with our current quest to explore Zn(II) complexes as potential TADF emitters, the probability of a further process in Scheme 1 attracts attention, namely the repopulation of the ^{1}LLCT state by rISC from the ^{3}LLCT state. Thus, the present joint theoretical and experimental study sets out to investigate the electronic structures and excited-state properties of such Zn(II) complexes to elucidate structure-property relationships for their possible application as TADF emitters.

Results and Discussion

We have chosen the previously studied complex [Zn(SC_6H_4-4-Cl)$_2$(phen)] (**1**) as model compound for an in-depth photophysical and theoretical study, and compare the findings with those obtained from further calculations for [Zn(SC_6H_4-4-Me)$_2$(phen)] (**2**) to elucidate the excited-state behavior of this general class of emitters.

Ground State and Absorption Properties

In contrast to Crosby et al., we have opted for THF as alternative solvent instead of $CHCl_3$/EtOH (1:19) to record the absorption due the higher solubility of **1** and because we experienced minor decomposition after prolonged irradiation in the original solvent combination. The appearance of the spectra at room temperature is identical to those previously reported albeit the absorption coefficients are slightly higher by a factor of ca. 1.5 (Figure 1).

The lowest energy absorption is very broad and found between λ_{abs} = 320–425 nm with low intensity (ε = 1,500 $M^{-1}cm^{-1}$), followed by a more allowed transition at λ_{abs} = 290 nm (ε = 19,000 $M^{-1}cm^{-1}$) and a high-intensity absorption with a maximum at λ_{abs} = 273 nm (ε = 60,000 $M^{-1}cm^{-1}$). Our concentration dependent measurements demonstrate that no ligand dissociation, aggregation or decomposition occurs that might interfere with the analysis of the photophysical data of the molecular species. The solid absorption shows the same general bands, although the infinite concentration results in

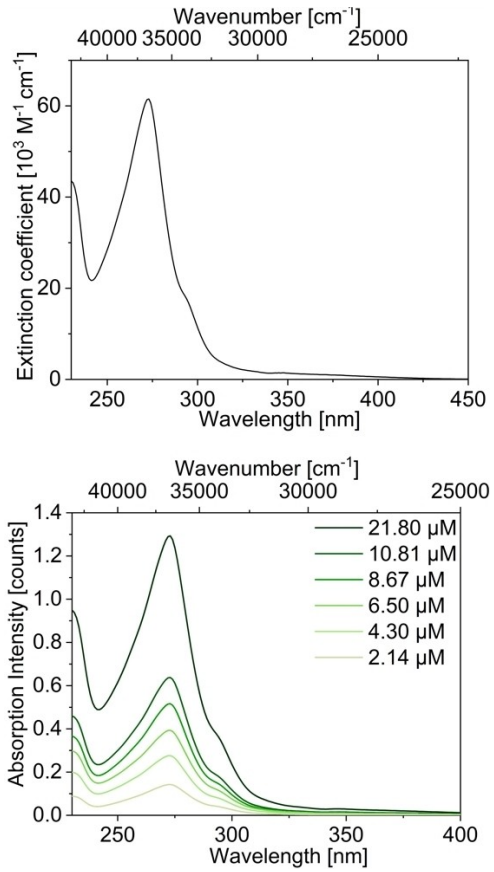

Figure 1. Concentration-dependent absorption spectra of [Zn(SC_6H_4-4-Cl)$_2$(phen)] (**1**) recorded in THF at room temperature.

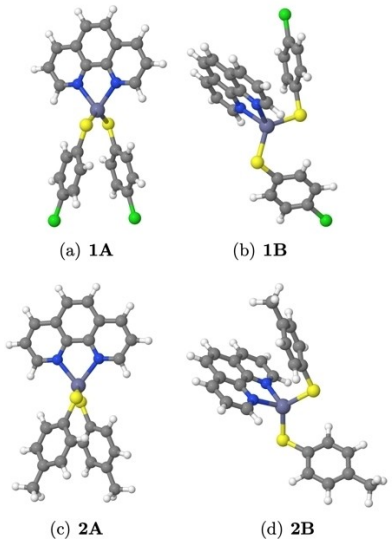

Figure 2. Computationally investigated conformers of complexes **1** and **2**.

significant vibrational broadening (Figure S4). However, it is important to note that in contrast to well-established photoactive Cu(I) phenanthroline complexes of the type [Cu(phen)(N^N/P^P/P$_2$)] (N^N = diimine, P^P = chelating phosphines, P = monodentate phosphines), which typically exist in only one conformation due to the steric bulk of the ligand sphere, the solution spectra represent an average over all conformers that can arise from rotation of the arylthiolate ligands, which also influence the luminescence behavior (*vide infra*).

Indeed, our calculations, using ethanol as solvent in the PCM implicit solvation model to account for the expected strong electrostatic solvent-solute interactions (see Methods), identified two major conformers in the ground state. One conformation is an open form with the arylthiolates arranged face-to-face and pointing away from the phen ligand (**1A**/**2A**) (Figure 2), as previously found for **1** in the single crystalline solid state by Cremers et al.[34] In the second conformer one of the arylthiolate ligand is backfolded towards the phenanthroline (**1B**/**2B**) which slightly destabilizes this nuclear arrangement in the electronic ground state by ca. 0.10 eV and should thus be accessible in the liquid phase. Due to the favorable Coulomb interaction between the donor and acceptor moieties after CT, the backfolded structures are preferred over the straight ones in the LLCT states, however (*vide infra*). Crystal structures of backfolded 1,10-phenanthroline zinc(II) bis(thiolate) complexes and methylated derivatives thereof were reported by Jordan et al.[26] and Scheins et al.[35] The X-ray analysis of single crystalline samples of **1** (Figure S3 of the Supporting Information) confirms a backfolded molecular structure in our solid-state experiments as well.[71]

Figure 3 shows the calculated absorption spectra of the two conformers of **1**. Corresponding spectra of **2** are displayed in

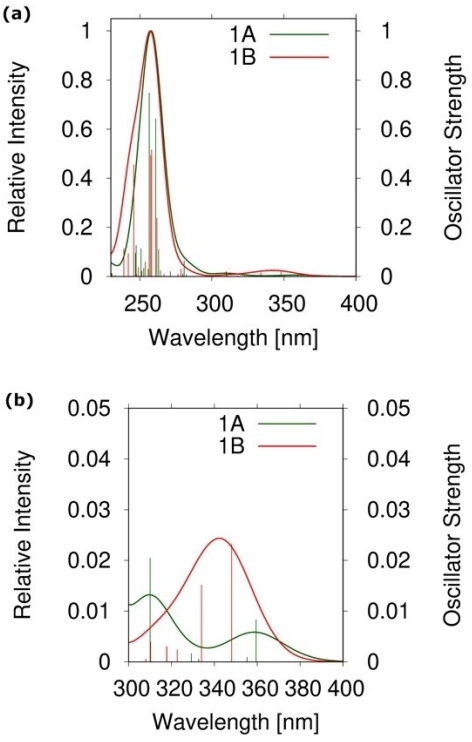

Figure 3. a) Calculated absorption spectra in implicit ethanol environment of conformers **A** (green) and **B** (red) of [Zn(SC_6H_4-4-Cl)$_2$(phen)] (**1**). b) Zoom in the low energy region.

Figure S8 of the ESI. Their envelopes were obtained by broadening the line spectra with Gaussians of 1000 cm^{-1} width and normalizing the intensity to the height of the peak in the 250–260 nm wavelength region. To get an impression of the intensity variations between the open forms **1 A** and **2 A** on the one hand and the backfolded conformers **1 B** and **2 B** on the other hand, the oscillator strengths of the spectral lines were left unscaled.

For all considered conformers, a broad peak in the short wavelength regime with a maximum at about 250–260 nm is found (Figures 3(a) and S8(a) of the ESI), which coincides well with the experimental results in solution (Figure 1 and Ref. [24]). The strongly absorbing states exhibit primarily LC character localized either on the phen or the thiolate ligands.

Their electron density differences are depicted for compound **1 A** in Figure 4 as S_{13} and S_{17}, respectively. Because the phen ligand is the same for all considered structures, the excitation wavelengths of its LC states vary only slightly among the compounds. The thiol-localized states are more sensitive with respect to the substituent in 4-position of the arene ring. For example, the most intense LC(thiolate) transition in **1 A** is bathochromically shifted with respect to the corresponding state in **1 B** by 0.16 eV and has only half the oscillator strength of the latter. CT contributions from sulfur lone-pair orbitals to the phen or thiolate π systems are found in nearly all transitions whereas contributions involving the Zn atom are negligible.

Much weaker transitions occur in the longer wavelength regime (Figure 3(b), Figure S8(b) in the Supporting Information). The maximum of the lowest-lying LC(phen) state, S_5 or S_6 depending on the specific compound and conformer (Figure 4), is rather constant at 305–310 nm. Interestingly, its oscillator strength is very conformation-dependent and one order of magnitude higher in the open form **1 A**/**2 A** than in the backfolded conformation **1 B**/**2 B**. In contrast, the position of the $S_1 \leftarrow S_0$ excitation of ^{1}LLCT nature is more ligand dependent and possesses a 3–5 times lower oscillator strength in the open forms **1 A** ($\lambda = 359$ nm, $f = 0.008$) and **2 A** ($\lambda = 378$ nm, $f = 0.005$) than in the backfolded conformers **1 B** ($\lambda = 348$ nm, $f = 0.023$) and **2 B** ($\lambda = 367$ nm, $f = 0.028$). These low-energy transitions agree nicely with the very weak and broad absorption band of $[Zn(SC_6H_4\text{-}4\text{-}Cl)_2(phen)]$ (**1**) in THF solution between 320–425 nm (Figure 1), which has also been found in other solvents and for other derivatives. Despite the good overall agreement between theory and experiment that supports the presence of conformers in solution and in the solid state, this comparison is not conclusive with regard to the population ratios of open **A** vs. folded **B**.

According to our analysis, at least one ^{3}LLCT state and one ^{3}LC (phen) state are found in the vicinity of the lowest ^{1}LLCT state in the FC region (see Tables 1 and 2). The electron density distributions of the ^{3}LLCT states are very similar to their singlet counterparts, as exemplified for compound **1 A** in Figure 5. Difference densities for the most relevant excited states of the

Table 1. DFT/MRCI excitation energies (ΔE/eV) of **1 A** in ethanol at various molecular geometries. The DFT/MRCI energy of the S_0 state at the DFT optimized S_0 minimum geometry in a polarizable ethanol environment serves as common origin. 0-0 energies including zero-point vibrational energy corrections are given in parentheses.

State	Optimized geometry			
	S_0	S_{LLCT}[a]	T_{LLCT}[a]	$T_{LC(phen)}$
S_0	0.00	0.39	0.53	0.35
S_{LLCT}	3.44	2.25 (**2.17**)	2.50	3.64
S'_{LLCT}	3.48	2.93	3.14	3.66
T_{LLCT}	3.38	2.17	2.35 (**2.24**)	3.60
T'_{LLCT}	3.43	2.89	3.06	3.63
T_{LC}	3.34	–	3.71	2.84 (**2.68**)
T'_{LC}	3.58	–	3.81	3.58

[a] Structure with one strongly elongated Zn-thiolate bond.

Table 2. DFT/MRCI excitation energies (ΔE/eV) of **1 B** in ethanol at various molecular geometries. The DFT/MRCI energy of the S_0 state at the DFT optimized S_0 minimum geometry in a polarizable ethanol environment serves as common origin. 0-0 energies including zero-point vibrational energy corrections are given in parentheses. The ground state of conformer **1 B** lies 0.11 eV above conformer **1 A** in implicit ethanol solution

State	Optimized geometry			
	S_0	S_{LLCT}	T_{LLCT}	$T_{LC(phen)}$
S_0	0.00	0.39	0.39	0.36
S_{LLCT}	3.56	2.11 (**2.05**)	2.11	3.78
S'_{LLCT}	3.71	2.82	2.82	3.94
T_{LLCT}	3.48	2.05	2.05 (**1.99**)	3.74
T'_{LLCT}	3.72	2.78	2.78	3.90
T_{LC}	3.37	3.59	3.59	2.82 (**2.66**)
T'_{LC}	3.58	3.66	3.66	3.56

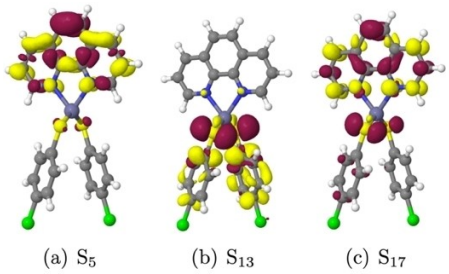

Figure 4. DFT/MRCI difference densities of the most prominent singlet LC excitations of compound **1 A** at the S_0 geometry in ethanol. Areas losing electron density in comparison to the electronic ground state are shown in red (isovalue −0.001), areas gaining electron density in yellow (isovalue +0.001).

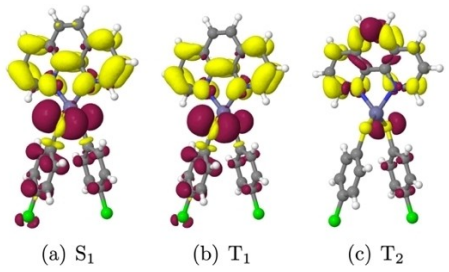

Figure 5. DFT/MRCI difference densities of the low-lying singlet and triplet excitations of compound **1 A** in ethanol at the S_0 geometry. For color codes and isovalues, see Figure 4.

other compounds are found in Figures S9-S14. The Zn ion does not appear to be involved in these low-lying excitations.

Note that the ^{3}LC (phen) wave function exhibits marked sulfur→phen CT contributions in the FC region, with consequences for its SOC ability (see below). The heavy-atom effect caused by the participation of the sulfur lone pair orbitals in the excitation of the ^{1}LLCT, ^{3}LLCT and ^{3}LC (phen) states in conjunction with their close energetic proximity opens the chance for substantial singlet-triplet mixing in the absorption region and could explain the branched triplet population kinetics. Indeed, we observe very strong SOC between different LLCT states in the FC region, designated by unprimed and primed symbols in Tables 1 and 2 (see also Tables S4 and S5 in the Supporting Information). In the open forms **1 A** and **2 A**, for example, the S_{LLCT} and T'_{LLCT} states are nearly degenerate. With values of 20.8 and 18.5 cm^{-1}, respectively, their mutual spin-component averaged SOCMEs are large enough to cause substantial mixing of singlet and triplet character. SOCMEs of similar magnitudes (21.6 and 19.0 cm^{-1}) are found for the S'_{LLCT} and T_{LLCT} pair of states.

Emission Properties

The emission spectrum of **1** in the solid state at 6.5 K shows three bands that vary in intensity in dependence of the temperature (Figure 6). A vibrationally resolved high energy band is observed between λ_{em} = 365–450 nm that has not been reported by Crosby et al., which we assign to residual fluorescence from a ^{1}LC (phen) state due to its very short lifetime of $\tau \ll 15$ ns. We exclude the presence of free 1,10-phenanthroline being responsible for this emission on the basis of our analytical characterization and the fact that its fluorescence would yield a much longer lifetime on the nanosecond timescale at such low temperatures. Also, the relative intensities of the fluorescence progressions compared to free phen at 13 K is significantly different (see Figure S5). Furthermore, very weak ^{3}LC (phen) emission occurs with λ_{em} = 455–480 nm and an additional very intense, broad and structureless band with an emission maximum at λ_{em} = 587 nm originates from a ^{3}LLCT state. While the intensity of the $^3\pi\pi^*$ band decreases between 6.5 K and 23 K, the ^{3}LLCT emission becomes more pronounced in that temperature range, which confirms that the higher energy ^{3}LC state thermally populates the lower energy state when an activation barrier is surmounted. At higher temperatures T > 23 K, the phenanthroline ligand phosphorescence is absent and enhanced non-radiative decay also reduces the emission intensity of the CT band. In contrast, Crosby et al. describe an increase in intensity of the ^{3}LLCT emission from 3 K to 35 K, but the difference might be explained as follows.

A comparison between measurements in rigid glass and crystals of the zinc(II) complexes revealed a different temperature-dependent behavior of the $^3\pi\pi^*$ band depending on the sample preparation: While the $^3\pi\pi^*$ band is still visible at 77 K in the rigid glass, it is completely quenched at 35 K in the crystal. As mentioned in the introduction, the different emission

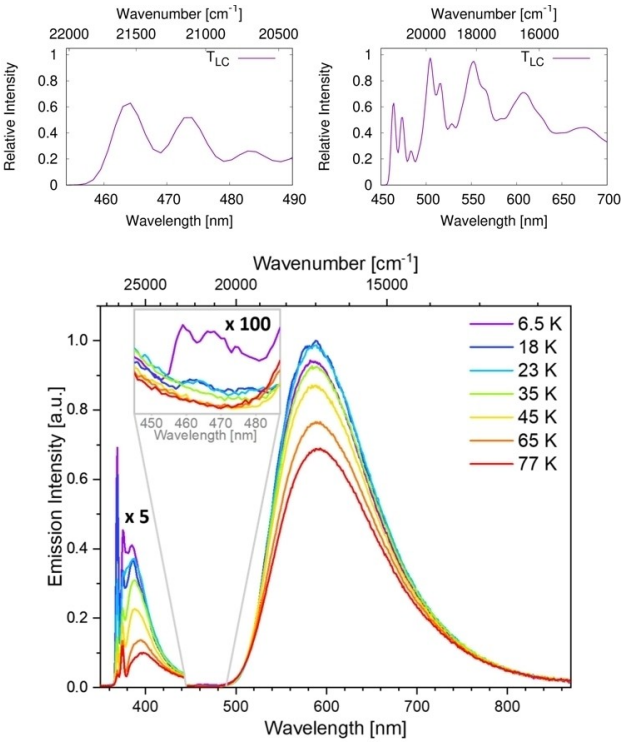

Figure 6. Bottom: Temperature-dependent emission spectra (λ_{Ex} = 320 nm) of a powdered sample of [Zn(SC_6H_4-4-Cl)$_2$(phen)] (**1**) recorded at 6.5–77 K, including expanded portions of the short-lived emission band emanating from the phen ligand and on the $^3\pi\pi^*$ band. Top: Computed $^3\pi\pi^*$ phosphorescence emission spectrum of conformer **1 A** (right) and expanded portion of the first major peak (left).

properties of a related complex in $P2_1/N$ vs. $P2_1/C$ crystal phases had led to the conclusion that geometrical restriction is a crucial factor effecting the energy barrier connecting LC and LLCT states (Scheme 1).[26,33] The most significant difference between the two crystal structures is the relative orientation of the thiolate ligands. Analysis of the reaction paths connecting the T_{LC} and T_{LLCT} minima (*vide infra*) furthermore suggest that large amplitude motion of one thiolate ligand promotes the internal conversion. Thus, assuming weaker geometrical restrictions in the powdered sample as a result of a less rigid environment, a faster population of the $^{1/3}$LLCT states and increase in intensity would be expected first. However, more facile non-radiative processes should then become dominant in the powder at lower temperatures than in the crystalline samples, which is what we observe. For further discussion of the emission process, it is important to note that neither the emission onset nor the offset shift when the temperature is raised to 77 K.

^{3}LC Emission

Time-resolved luminescence measurements reveal for the ^{3}LC emission at 6.5 K a tri-exponential decay with a shorter lifetime of τ_{av} = 274 ms than the earlier value of the mono-exponential τ = 390 ms, but the intensity was too low to reliably determine

the lifetime for higher temperatures although Crosby et al. reported a lifetime of 40–45 ms even at 23 K. The short lifetime component is presumably due to tunneling through the barrier connecting the ^{3}LC and LLCT potentials (*vide infra*).

Vibronic ^{3}LC phosphorescence spectra of **1 A** are displayed in Figure 6 top. Very similar spectra are obtained for **1 B**, **2 A** and **2 B** (see Figures S15–S17). Their 0-0 energies range between 2.67 and 2.71 eV (21,500–21,900 cm^{-1}), in excellent agreement with experiment. Highland et al.[28] assumed the first vibrational peak to be the band origin and reported onsets of 21,800 cm^{-1} and 21,200 cm^{-1} for the $^3\pi\pi^*$ luminescence of **1** and **2**, respectively. According to our calculations, the pronounced vibrational progressions can predominantly be associated with a stretching vibration of the C_5-C_6 bond of the phenanthroline backbone ($\nu = 1{,}760$ cm^{-1} in the S_0 state) and a bending vibration of the N_1–Zn–N_{10} bite angle ($\nu = 441$ cm^{-1} in the S_0 state). The highest maxima in the calculated phosphorescence spectra are the second peaks at about 20,000 cm^{-1}. Both, the shapes and peak positions, match very well with a low-temperature luminescence spectrum of the [$ZnCl_2$(phen)] complex where the LLCT states are absent.[28] Computed component-averaged radiative lifetimes of the ^{3}LC(phen) phosphorescence range from about 3 s for **1 A** and **1 B** to about 2 s for **2 A** and **2 B**. These are typical values for a pure $^3\pi\pi^*$ emission, but they are about an order of magnitude larger than the experimentally determined lifetimes of the blue-green emission at 6.5 K. One explanation for the difference between measured and computed lifetimes is the FC approximation applied in the calculations. Coupling between vibrational and electronic degrees of freedom is known to enhance the probability of weak spin-forbidden transitions.[62–65] Another explanation takes account of the fact that the energy barrier for the ^{3}LC⇝^{3}LLCT internal conversion is very low suggesting that the measured lifetimes entail contributions from non-radiative deactivation channels.

On the basis of TME experiments, Highland et al. estimated a barrier height of ≈140 cm^{-1} for the migration from the $^3\pi\pi^*$ to the LLCT potentials.[28] Qualitatively, our calculations support the conclusions that a thermally surmountable barrier exists between the ^{3}LC and ^{3}LLCT potentials. An upper bound for the energy barrier of the open forms was obtained by calculating energy profiles along linearly interpolated paths connecting the optimized $^3\pi\pi^*$ (phen) and LLCT geometries (Figures 7 and S18 of the Supporting Information). The electronic energy differences between the intersections of the triplet potentials and the respective ^{3}LC minima yields barrier heights of 350 cm^{-1} for **1 A** and 225 cm^{-1} for **2 A**. Both values are somewhat larger than the experimentally estimated energy barrier of 140 cm^{-1}, but still in the right ballpark.

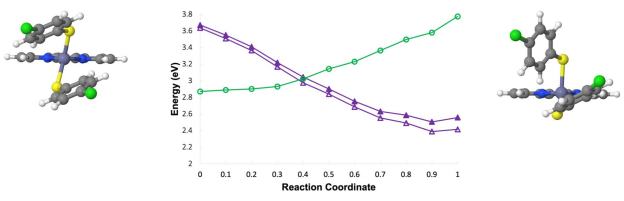

Figure 7. DFT/MRCI energy profiles of **1 A** (middle) in implicit ethanol environment along a linearly interpolated path connecting the connecting the T_{LC} minimum (reaction coordinate 0) with the T_{LLCT} minimum (reaction coordinate 1). Filled symbols: singlets, unfilled symbols triplets, violet: LLCT, green: LC $^3\pi\pi^*$ (phen). Orientation of the thiolate ligands at the T_{LC} minimum geometries (left) and at the intersection between the T_{LC} and T_{LLCT} potentials (right).

To get an idea how the barrier height could possibly be manipulated by chemical substitution, we analyzed the intrinsic reaction coordinate of this transformation. A detailed list of geometry parameters can be found in Tables S4–S9 of the Supporting Information. With regard to the energy, the influence of the substituents in 4-position of the thiol ligands is small, but not negligible. The +I-effect of the Me group leads to slight shifts of the T_{LC} and T_{LLCT} excitation energies in comparison to the chlorinated compound. These shifts have the effect that the crossing between the LC $^3\pi\pi^*$ (phen) state and the LLCT lies in closer proximity to the T_{LC} minimum and that the energy barrier is marginally lower in complex **2 A** than in complex **1 A** (compare Figure 7 and Figure S18). All in all, the effect of the substitution on the energy paths is rather small, however. The geometrical changes in the orientation of the thiol groups have a much stronger influence on the energies than the electronic contributions of the methyl and chloro groups. As described before, the electron hole localizes on one of the two thiolate ligands upon LLCT excitation. The most eye-catching geometry change along the reaction paths relates to the torsion angle of this donor thiolate. The other thiolate ligand does not significantly contribute to the charge transfer and therefore does not undergo substantial geometrical adjustments. While both thiolate ligands are nearly π-stacked in the T_{LC} states of the open forms (Figure 7 left; Figure S18 left), one of them is substantially displaced and the Zn–S bond of this ligand is markedly elongated upon transition from the ^{3}LC to the LLCT geometries (Figure 7 right; Figure S18 right). These geometry changes have only a marginal effect on the T_{LC} state, but they lead to a substantial stabilization of the LLCT states. At the intersection of the triplet potentials, the Zn–S bond is elongated by 0.19 Å in complex **1 A** and by 0.11 Å in complex **2 A** compared to the nuclear arrangements at their respective T_{LC} minima. To hamper the interconversion between the T_{LC} (phen) and LLCT states, it might therefore be advisable to involve a bidentate dithiolate ligand instead of two monodentate thiolate ligands.

Comparison of our experimental data with reported lifetimes shows a distinct difference at low temperatures: At 6.5 K we obtain a much shorter value of $\tau_{av} = 394$ μs (vs. $\tau = 8$ ms), while at 35 K our measured lifetime of 151 μs is similar to the previous one of 130 μs. It is possible that in our case the different sample preparation might lead to a less rigid environment with a lower energy barrier for the rate-determining ^{3}LC⇝LLCT transitions, consequently resulting in faster population of the LLCT states at lower temperatures.

LLCT Emission

The ^{3}LLCT lifetimes could be determined by averaging over a tri- or bi-exponential decay, of which the respective components vary between 6.5–297 K (see Table S2 of the Supporting Information). However, we note that we could not reproduce an additional fast lifetime of <15 ns that has previously been observed at all temperatures and rationalized as prompt fluorescence from the ^{1}LLCT state following direct population of this state by the laser pulse (*vide infra*). Our attention was caught by the fact that the average lifetime follows a sigmoidal trend upon raising the temperature, starting with small fluctuations between 6.5 K (394 µs) and 23 K (417 µs) followed by a distinct decline to a value of 4.42 µs at 77 K with an associated averaged radiative rate constant of $k_{r,77K}=\Phi_{em}/\tau_{av}=7.7\times10^4\ s^{-1}$ ($\Phi_{em,77K}=0.34$) (Figure 8). The lifetime then further decreases exponentially to a value of 80 ns at room temperature, while the experimentally determined quantum yield of the LLCT band shows a linear trend, suggesting that both the non-radiative (k_{nr}) and the radiative rate constants (k_r) change. Such a behavior is typical for multiple-state emission as found in TADF (TADF = thermally activated delayed fluorescence) emitters, which would be a very attractive mechanism for Zn(II) complexes to obtain high radiative rate constants as it bypasses the spin-forbidden phosphorescence.

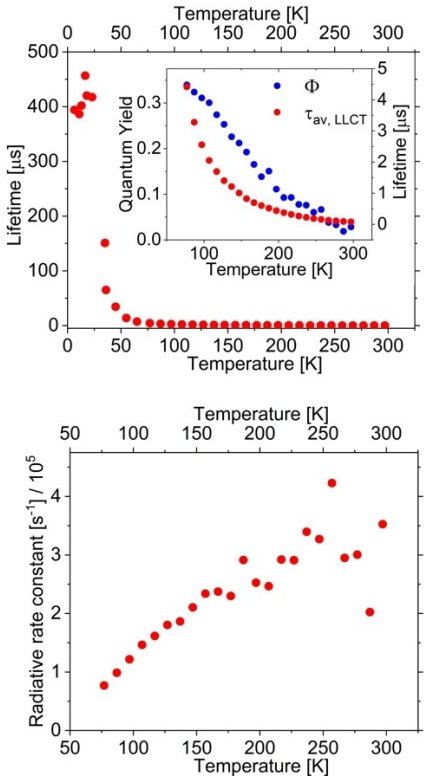

Figure 8. Temperature-dependent averaged observed emission lifetime (red) and quantum yield (blue) (top), and resulting averaged radiative rate constant $k_{r,av}$ (bottom) of the LLCT emission band of [Zn(SC_6H_4-4-Cl)$_2$(phen)] (**1**) in the solid state.

Evaluation of the temperature-dependence of k_r usually allows to determine the critical excited state parameters of the TADF process by using Eq. (1) for a three-state-model:[40]

$$\tau_{r,av}=\frac{3+\exp\left(-\frac{\Delta E(S_1-T_1)}{k_BT}\right)}{\frac{3}{\tau(T_1)}+\frac{1}{\tau(T_1)}\exp\left(-\frac{\Delta E(S_1-T_1)}{k_BT}\right)} \quad (1)$$

where k_B is the Boltzmann constant, $\tau(S_1)$ and $\tau(T_1)$ are the radiative decay times of the singlet and triplet excited states, respectively. In this case, it is important to note that the multi-exponential lifetime decay is the result of the properties of the overall solid state sample and provides only an average single lifetime τ_{av}, from which only a $k_{r,av}$ can be determined by measuring the steady state quantum yield Φ of the overall sample. However, the TADF parameters such as $\Delta E(S_1–T_1)$, $\tau(S_1)$ and $\tau(T_1)$ are typically related to a single specific molecular structure. The origin of the multiple lifetime components and their absolute contributions to Φ are unknown, and could be the result of different conformers in the solid state, or of various specific environments and intermolecular interactions. Consequently, some assumptions are necessary in order to reasonably approximate $k_{r,av}$ from the observed τ and Φ. Firstly, the respective emitting states that generate the multiple lifetimes all participate in the same general mechanism. Secondly, their extinction coefficients are not temperature-dependent, which is justified as we have chosen an excitation wavelength in the UV, where $\pi\pi^*$ transitions occur and differences in conformation usually do not play a role. Thirdly, due to the CT character of the emission band and absence of any shoulders, the contributions of the lifetimes do not depend significantly on λ_{em}, which we have confirmed experimentally for a few temperatures. Thus, it is justified to relate the quantum yield from the steady state spectrum to τ_{av} observed at only one emission wavelength. Unfortunately, since the quantum yield is not temperature-independent and our equipment allows measurement of Φ only between 297–77 K, we cannot determine $k_{r,av}$ and $k_r(T_1)$ at lower temperatures. We have therefore simulated two scenarios for $T<77$ K to estimate a range for the energy difference $\Delta E(S_1–T_1)$ and clarify the feasibility for TADF: a) Φ remains constant at 0.35 or b) linear increase of the quantum yield to reach $\Phi=0.50$ at 25 K following the trend in Figure 8 (see also Table 3 and Figures S6–S7 of the Supporting Information).

Both scenarios yield rather low values for $\Delta E(S_1–T_1)$ of 242 and 247 cm^{-1} for PLQY of 35 % and 50 %, respectively, that are sensible considering the LLCT character of the involved states and absent temperature-dependent shift of the emission onset, which make a TADF process appear feasible. The radiative

Table 3. Calculated TADF parameters for **1** based on the fitting procedure [Eq. (1)].

	$\Delta E(S_1–T_1^{I,II,III})$ [cm^{-1}]	$\tau_r(S1)$ [ns]	$\tau_r(T_1^{I,II,III})$ [µs]
"35 %"-Scenario	247 ± 80	4 ± 14	1181 ± 16
"50 %"-Scenario	242 ± 48	20 ± 38	828 ± 12

lifetime of the emitting triplet state is very long with ca. 1 millisecond ($k_{ph} = 8\times10^2/1.2\times10^3\ s^{-1}$) and coincides with an expected weak SOC between the ^{3}LLCT state and S_n states that could provide oscillator strength (see below). Although the prompt fluorescence lifetimes $\tau(S_1)$ are in a range typical for TADF emitters to outcompete phosphorescence from the T_1 state after $T_1 \rightsquigarrow S_1$ rISC, they are certainly too short bearing in mind the enormous CT distance and resulting orbital overlap forbiddance of the transition $S_1 \rightarrow S_0$, which is also displayed in the very small extinction coefficient of the absorption. We explain this with the kinetic scheme underlying the typical TADF fit routine (Eq. (1)) requiring $k_{ISC} \gg k_{rISC}$ and both to be faster than either fluorescence k_f or phosphorescence k_{ph}, so that S_1 and T_1 can equilibrate before light emission. In addition, non-radiative decay to the electronic ground state is assumed to be markedly slower than radiative decay. The very low $\Delta E(S_1–T_1)$ and nearly non-existing transition orbital overlap can lead to $k_{ISC} \simeq k_{rISC}$ and a very small fluorescence rate constant k_f, which might then be on the timescale of k_{ISC}. Consequently, the observed rate constant k_{TADF} of $3.5\times10^5\ s^{-1}$ at room temperature is then very similar to k_f, giving an estimated $\tau_r(S_1)$ of 2.9 µs (*vide infra*). Again, we emphasize that these calculated values have to be treated with care as this analysis is based on approximations, but nevertheless are quite helpful to evaluate the probability of TADF.

While information about the non-radiative vs. radiative deactivation pathways is available through the measured luminescence quantum yields, ISC and rISC rate constants are not directly accessible from experiment and are computed as follows. The zero-field splittings of the T_{LLCT} sublevels are minuscule (well below 1 cm^{-1}). In that case, the rate constant for singlet-triplet ISC or triplet-singlet rISC from a thermally equilibrated initial electronic state Ψ_a to a final state Ψ_b is given by Equation (2):

$$k^{FC}_{(r)ISC,ab} = \frac{2\pi}{\hbar g_a Z_a} \underbrace{\sum_{\gamma_b}^{g_b}\sum_{\gamma_a}^{g_a} \left|\langle \Psi_{b,\gamma_b}|\hat{\mathcal{H}}_{SO}|\Psi_{a,\gamma_a}\rangle\right|^2}_{\text{electronic SOCME}} \underbrace{\sum_w \sum_v e^{-\beta(E_{a,v}-E_{a,0})} \left|\langle \chi_w|\chi_v\rangle\right|^2 \delta(E_{a,v}-E_{b,w})}_{\text{FCWDOS}} \quad (2)$$

in FC approximation. Herein, g_a and g_b denominate the number of degenerate fine-structure components, v and w the vibrational wavefunctions χ associated to the electronic states Ψ_a and Ψ_b states, respectively, and Z_a is the canonical partition function of vibrational motion in the initial state, defined as [Eq. (3)]:

$$Z_a = \sum_v e^{-\beta(E_{a,v}-E_{a,0})} \quad (3)$$

with $E_{a,0}$ representing the zero vibrational energy of the intial state and $\beta = 1/k_BT$. The Fermi golden rule expression Eq. (2) is essentially determined by three factors:[39] The electronic SOCME, the FCWDOS and the temperature. The spin-component averaged electronic SOCME between the initial and final electronic states enters this equation quadratically. The vibrational density of final states at the energy of a particular vibrational level in the initial electronic state depends upon the geometric and energetic displacements of the respective minima and the vibrational frequencies. The temperature determines the probability of finding the molecule in a particular initial state (partition function Z_a) and broadens the energetic window in which a matching pair of initial and final states can be found in the FCWDOS (delta function).

Rate constants for fluorescence and spin component-averaged phosphorescence have been determined in FC approximation according to Equation (4):

$$k_r^a = \frac{\Delta E_a^3}{3\pi\varepsilon_0\hbar^4c^3g_a} \sum_{\gamma_a}^{g_a} \left|\langle \Psi_0|\hat{\mu}|\Psi_{a,\gamma_a}\rangle\right|^2, \quad (4)$$

where $\hat{\mu}$ is the electric dipole operator and $\Delta E_a$is the vertical energy of the electronic state a at its optimized geometry. Ψ_a and Ψ_0 are spin-orbit mixed DFT/MRSOCI wavefunctions of the inital and ground states, respectively. Therefore, Eq. (4) is equally applicable to fluorescence and phosphorescence. The separation of vibrational and electronic degrees of freedom, i.e. the FC approximation, is usually well justified in the case of strong fluorescence emission. In typical TADF emitters with (nearly) perpendicular donor and acceptor moieties and small transition dipole moments, however, vibronic interaction is known to accelerate the fluorescence substantially. Computationally, such interactions have been incorporated either by means of a Herzberg-Teller expansion of the transition dipole moment[41,42] or by addition of derivative coupling terms arising from the nuclear kinetic energy operator.[43] The good agreement between our experimental and computed fluorescence rate constants (*vide infra*) shows that vibronic coupling terms are of minor importance for the S_{LLCT} fluorescence of **1**. They are expected to enhance the weak ^{3}LC phosphorescence, however. We have nevertheless refrained here from evaluating these spin-vibronic interactions because they are computationally very expensive but not decisive for the TADF properties of the complexes.

All dithiolate complexes investigated in our computational study undergo large-amplitude displacements of the thiolate ligands upon geometry relaxation in the respective LLCT state, thereby releasing substantial excess energy with regard to the FC point. As the electronic and nuclear structures of the S_{LLCT} and T_{LLCT} states closely resemble one another, we only display difference densities of the T_{LLCT} states of **1 A** and **1 B** in Figure 9.

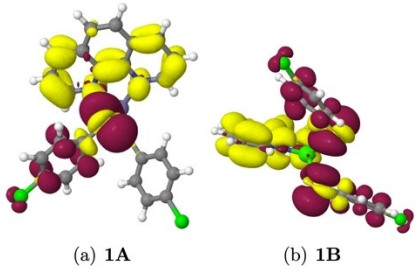

Figure 9. DFT/MRCI difference densities of the T_{LLCT} states at the optimized T_{LLCT} geometries of **1** in implicit ethanol solution. For color codes and isovalues, see Figure 4.

Corresponding difference densities of compound **2** may be found in Figure S19 of the Supporting Information.

The most attractive nuclear arrangement appears to be a folded structure in which one thiolate ligand is placed at an angle with respect to the phen ligand and the other one points away from it. It represents the potential well into which the S_1 states of conformers **1 B** or **2 B** relax after electronic excitation. Here, electron density is transferred from both thiolate groups to the phen ligand. The corresponding T_{LLCT} minima can be found by starting from the optimized S_{LLCT} geometries and searching for the lowest triplet excited state (Figures 9(b) and S19(b) of the Supporting Information). A complication arises when the geometry optimization of the S_1 state is started from the FC point of the stretched-out conformers **1 A** or **2 A**. In this case, a minimum cannot be found for a face-to-face alignment of the thiolates. Due to electrostatic repulsion of the positively charged thiolate residues, one ligand starts rotating about the Zn–S bond and moves toward the negatively charged phen ligand (compare Figures 5 and 9). The excitation then localizes and only one thiolate ligand participates in the LLCT excitation. Moreover, the Zn–S bond of this ligand is elongated to an extent (2.83 Å for **1 A** and 2.69 Å for **2 A**, compared to 2.31 Å in the respective electronic ground state) that it can be considered effectively broken. In densely packed environments such as the crystalline state or rigid glasses, large-amplitude torsional and bending motions of the thiolate ligands are hindered by neighboring molecules.[44] Because the potential energy surfaces are very shallow with respect to torsion and bending angles involving the sulfur atoms of the donor moieties, these geometry restraints are not expected to cause significant energy penalties in the excited state. A comparison of the calculated adiabatic excitation energies with the experimental onsets of the LLCT emission may therefore be meaningful whereas vertical emission energies at the excited-state minimum geometries are not expected to match with the maxima of the broad LLCT emission bands. Furthermore, we expect the large-amplitude displacement of the thiolate ligand to substantially affect the dipole transition moment and the FC overlaps. We have therefore refrained from computing vibronic spectra of the **A** conformers.

Our experimentally measured broad LLCT band of **1** (Figure 8) has an onset between 20,000 cm^{-1} and 19,000 cm^{-1}, in agreement with previous estimates by Highland *et al.*[28] who assigned the positive phase of a TME spectrum to the ^{3}LLCT emission of **1**. For **2**, the onset of this band lies between 18,000 cm^{-1} and 17,000 cm^{-1} according to these authors. Hence, the calculated adiabatic LLCT excitation energies of the chlorinated conformer **1 A** (Table 1) and the methylated compound **2 A** (Supporting Information Table S4) fit reasonably well. Inspection of Table 2 (and Table S4 of the Supporting Information) reveals that the adiabatic T_{LLCT} and S_{LLCT} energies of their folded counterparts **1 B** and **2 B** are lower. This is true even on an absolute scale when the relative energies of the conformers in their electronic ground states are taken into consideration. In view of these results, we therefore suppose that the **A** conformers fold upon LLCT excitation in liquid solution whereas they are hindered to undergo this transformation and to lose a thiolate ligand in the crystalline state.

Our calculated rate constants for radiative and nonradiative transitions of the LLCT states of the **B** conformers are collected in Table 4. The computed 0-0 energy splitting of the S_{LLCT} and T_{LLCT} (423 cm^{-1}) matches well with the experimental estimates obtained according to Eq. (1) based on fits of the temperature dependence for quantum yields ranging between 0.35 and 0.5 (Table 3). We refrained from computing rate constants for the **A** forms because they are conformationally very flexible and do not provide reliable potential energy surfaces for such an endeavor.

In the cryogenic temperature regime close to 0 K, only fluorescence, ISC and phosphorescence need to be considered because rISC is too slow to repopulate the S_{LLCT} state and internal conversion to the S_0 state is not very probable at these temperatures. ISC outcompetes fluorescence by a factor of about 50–100 according to our calculations (see Table 4). We note that the mutual interactions of the LLCT and ^{3}LC states do not influence the TADF process at room temperature due to the high adiabatic energy differences of 0.67 and 0.86 eV for **1 B** and **2 B**, respectively.

The calculated radiative lifetimes of the LLCT fluorescence (3.4–4.3 μs), obtained from the probabilities of spontaneous $S_1 \rightarrow S_0$ emission at the S_{LLCT} geometry according to Eq. (4), are in the typical μs range observed in CT emissions of donor-acceptor compounds and agree very well with the 2.9 μs radiative lifetime derived from our experimental data (*vide supra*). The involvement of the sulfur atom in the LC and LLCT excitations does not only explain the branched triplet population kinetics observed in experiment, it also leads to sizable intensity borrowing from higher-lying bright states. The

Table 4. 0-0 energy splittings ΔE_{S-T} and spin component-averaged S_{LLCT}–T_{LLCT} SOC [cm^{-1}] and radiative as well as nonradiative rate constants k [s^{-1}] of the LLCT states of compounds **1 B** and **2 B** computed according to Equations (2)–(4).

	ΔE_{S-T}	S_{LLCT} k_F	SOC	T_{LLCT} k_P	SOC	Temperature T[K]	k_{ISC}	k_{rISC}
1 B	423	2.9×10^5	0.26	1.1×10^2	0.30	298	2.0×10^7	1.3×10^7
						77	2.8×10^7	1.6×10^4
						35	2.8×10^7	3.1×10^0
						10	1.1×10^7	–
2 B	472	2.3×10^5	0.38	1.5×10^2	0.64	298	7.1×10^5	2.8×10^5
						77	5.3×10^6	2.4×10^3
						35	2.9×10^5	0.1×10^0
						10	2.9×10^5	–

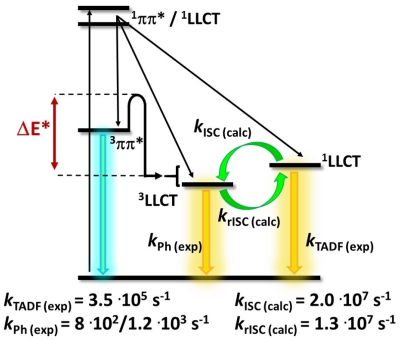

Scheme 2. Excited-state decay mechanism upon photoexcitation of [Zn-$(SC_6H_4$-4-Cl$)_2$(phen)] as proposed in this work.

calculated T_{LLCT} phosphorescence lifetime of 9 ms (see Table 4) is, however, approximately an order of magnitude longer than the radiative T_{LLCT} lifetimes estimated from our temperature-dependent spectra on the basis on Eq. (1). Note that the theoretically and experimentally derived radiative lifetimes entail uncertainties associated with the large-amplitude motion of the thiolate ligand on the theoretical side and the limitation of the PLQY measurements to the temperature range between 297 and 77 K on the experimental side. The calculated phosphorescence lifetime fits well to the LLCT lifetime of complex **1** of 8 ms at 6.5 K, assigned to phosphorescence by Highland *et al.*,[28] which evolves to 0.66 ms when the temperature is raised to 23 K and which decreases to 0.13 ms at 35 K to 4.2 μs at 77 K. Phosphorescence is too slow, however, to explain the experimentally determined μs decay times at 77 K.

Due to the small singlet-triplet energy gaps ΔE_{S-T} and the internal heavy atom effect of the sulfur atoms, rISC appears to be sufficiently fast to repopulate the S_{LLCT} state even at liquid nitrogen temperature. At room temperature, the ISC and rISC rate constants of **1B** have nearly equal magnitudes and are about 40–70 times larger than the pure radiative lifetimes. The excited singlet and triplet populations will therefore equilibrate, given that non-radiative deactivation by internal conversion to the electronic ground state does not dominate. Hence, we associate the averaged LLCT lifetime of 2.9 μs of our powdered sample of complex **1** (*vide supra*) with the lifetime of delayed fluorescence.

Summary and Conclusion

In this work, extensive quantum chemical and spectroscopical studies have been performed to elucidate the photophysical decay mechanisms of Zn(II) bis-thiolate diimine complexes and their potential suitability as triplet harvesters in electroluminescent devices. For [Zn$(SC_6H_4$4-R$)_2$(phen)] (R=Me, Cl), temperature-dependent dual luminescence in organic glass and in the crystalline solid state had been reported by Crosby and coworkers.[24–28] The vibrationally structured high-energy band had been assigned to phosphorescence from a phenanthroline-centered locally excited $^3\pi\pi^*$ state and the broader lower-energy band to interligand thiolate→phen LLCT transitions. The results of our study in principle support the kinetic scheme proposed by Crosby *et al.*, but add an efficient reverse intersystem crossing (rISC) channel allowing the upconversion of ^{3}LLCT population to the ^{1}LLCT state at room temperature (Scheme 2). The heavy-atom effect caused by the participation of sulfur orbitals in the excitation of the ^{1}LLCT, ^{3}LLCT and ^{3}LC (phen) states in conjunction with their close energetic proximity opens the chance for substantial singlet-triplet mixing in the absorption region and rationalizes the branched triplet population kinetics observed in experiment. While weak phosphorescence from the ^{3}LC (phen) state dominates the short-wavelength emission, the red-shifted ^{3}LLCT emission is visible even at cryogenic temperatures. At room temperature, efficient ^{1}LLCT⇔^{3}LLCT ISC and rISC leads to quick equilibration of the singlet and triplet populations making thermally activated delayed fluorescence (TADF) the major emission channel.

Upon population of the LLCT states, one of the thiolate ligands starts to fold back toward the phen ligand due to the Coulomb attraction between electron hole and particle and the high conformational flexibility of the monodentate thiolate ligands. The large-amplitude motion in the LLCT states does not only have the consequence that the emission spectrum becomes very broad, it also makes the complex susceptible to photodissociation of the ligand because it is accompanied by substantial elongation of its Zn–S bond. To increase the color purity of the emission and the photostability of the complex, containment of the thiolate ligand flexibility therefore appears mandatory. Such a containment should be possible even in non-rigid environments if a bidentate dithiolate ligand is employed instead of two monodentate thiolates. Moreover, photolability issues could be mitigated by shifting the absorbance from the UV to the visible wavelength region. A study investigating the photophysical properties of fourfold-coordinated Zn(II) complexes involving bathochromically shifted phen derivatives as acceptors and bidentate dithiolates as donor ligand is currently under way. In a subsequent contribution, we will also report on the excited state behavior of the hemicage compound ZnL_3 where rigidification has been achieved by linking the three bipyridyl ligands via ethyl bridges to a mesityl core.

Experimental Methods

The zinc complex **1** has been synthesized according to an established procedure[25] and its identity and purity confirmed by elemental analysis, single-crystal X-ray diffraction, and multinuclear NMR spectroscopy (see the Supporting Information). Sample preparation was carried out under argon using glovebox techniques. Microcrystalline powder samples have been prepared by 10-fold grinding of the single-crystalline material with mortar and pestle. UV-Vis absorption spectra were measured on an Agilent Cary 5000 using standard 1 cm path length quartz cells, or a Praying Mantis set-up for solid state measurements. Emission and excitation spectra were recorded on an Edinburgh Instrument FLS1000 equipped with a 450 W Xenon arc lamp, a red sensitive photomultiplier (PMT-980) as the detector and double monochromators for the excitation and emission pathways. The emission was

collected at right angles to the excitation source with the excitation wavelength selected by a double grated monochromator and detected by the respective PMT. The recorded emission and excitation spectra were corrected using the standard corrections supplied by the manufacturer for the sensitivity of the detector and the spectral power of the excitation source. Luminescence lifetimes were measured either using a μF2 60 W Xenon Flashlamp and multichannel scaling module (MCS) or with a variable pulsed LED (VPLED) and MCS. The quantum yields were measured using a Cryosphere and the mentioned FLS1000. Low temperature measurements were performed in an Advanced Research System closed cycle 4 K Cryostat equipped with a water-cooled helium compressor.

Computational Methods and Technical Details

The Gaussian 16 program package[45] was used for all geometry optimizations. The equilibrium geometries of the electronic ground states were determined with Kohn-Sham density functional theory (DFT).[46] Unless stated otherwise, the BH-LYP functional[47,48] functional[49,50] in conjunction with dispersion corrections[51] was used herein. For singlet excited-state geometries, time dependent DFT (TDDFT)[52] calculations were performed while the Tamm-Dancoff approximation (TDDFT-TDA)[53] was employed for the geometry optimization of the triplet states. With the exception of sulfur, all nonmetal atoms were represented by the def-SV(P) basis set[54] from the Turbomole basis set library. The def2-SVPD basis sets on sulfur and chlorine differ from the def-SV(P) basis by the addition of a diffuse *s*, *p*, and *d* function, respectively. For the Zn ion a relativistic small-core effective core potential[55] and the associated contracted 6s5p3d basis set were employed.

The Zn(II) diimine dithiolate complexes are very polar molecules in their electronic ground states, with static dipole moments of up to 25 D. The polarity of the matrix or solvent environment is thus expected to have large impact on their photophysical properties. Self-consistent reaction field calculations employing the polarizable continuum model PCM[56,57] were performed with the Gaussian 16 package[45] and point charges were exported for further use in subsequent multireference configuration interaction (MRCI) calculations of the spectral properties. The stationary points of the DFT and TDDFT potentials were verified as minima through a vibrational analysis using analytic second derivatives implemented in Gaussian 16.[45] The resulting normal mode frequencies and coordinates were further utilized to generate Franck-Condon (FC) factors and FC-weighted densities of states (FCWDOS) for determining spectral profiles and rate constants, respectively.

Kohn-Sham orbitals of the closed-shell ground-state determinant and three-index two-electron resolution-of-the-identity approximated integrals for subsequent DFT/MRCI calculations were generated with the Turbomole program package[58,59] simulating the solvent environment by importing the pre-computed field of point charges. Electronic excitation energies and oscillator strengths of the spin-allowed transitions were calculated with the DFT/MRCI method[60,61] employing the redesigned R2018 Hamiltonian parameterized for transition metal compounds.[62] Due to the size of the complexes, a tight configuration selection criterion (threshold 0.80 E_h) was used throughout. The DFT/MRCI secular equations were solved for 30 singlet and 30 triplet roots.

Electronic spin-orbit coupling matrix elements (SOCMEs) for the evaluation of intersystem crossing (ISC) rate constants were obtained with the SPOCK program.[63,64] The effective spin-orbit coupling (SOC) one-electron Hamiltonian comprised a relativistic ECP[55,65] on zinc and an atomic mean-field approximation of the Breit-Pauli spin-orbit operator[66,67] on all other centers. Phosphorescence lifetimes were computed using the variational multireference spin-orbit configuration interaction (MRSOCI) method.[68] The individual phosphorescence rate constants were averaged over the three triplet components as the zero-field splittings are small. Rate constants for ISC and reverse ISC (rISC) at a given temperature were obtained in FC approximation assuming a Boltzmann population of the vibrational levels in the initial state. The FCWDOS, needed – in addition to the electronic SOCMEs – for the computation of the ISC rate constants, was calculated via a fast Fourier transformation ansatz employing the Vibes program.[69,70] Before numerical integration using 65536 grid points in an interval between 0 and 300 fs, the time correlation function was damped by a Gaussian function of width 100 cm^{-1}.

Supporting Information Available

Details of the sample preparation, elemental analysis and crystal structure of complex 1; fit parameters of the measured lifetimes at various temperatures; computed absorption spectra and vertical as well as adiabatic excitation energies of compounds **2 A** and **2 B**; computed phosphorescence spectra and difference densities of selected electronic states of **1 B**, **2 A** and **2 B**; energy profiles of **2 A** along a linearly interpolated path connecting the ^{3}LC (phen) and LLCT minima; chemical structures of the zinc(II) thiolate complexes with atom numbers, selected geometry parameters of the complexes **1 A** and **2 A** along the linearly interpolated paths connecting the ^{3}LC (phen) and LLCT minima; Cartesian coordinates of all optimized stationary points of the complexes **1 A**, **1 B**, **2 A** and **2 B**.

Acknowledgements

This work was supported by Deutsche Forschungsgemeinschaft [DFG, Priority Program SPP 2102 "Light-controlled reactivity of metal complexes" (MA 1051/18-1 and STE 1834/7-1)]. Open Access funding enabled and organized by Projekt DEAL.

Conflict of Interest

The authors declare no conflict of interest.

Data Availability Statement

The data that support the findings of this study are available in the supplementary material of this article.

Keywords: density functional calculations · excited states · phosphorescence · thermally amplified delayed fluorescence · zinc

[1] E. Zysman-Colman (Ed.), *Iridium(III) in Optoelectronic and Photonics Applications*, John Wiley & Sons, Ltd. **2017**.

[2] H. Yersin (Ed.), *Highly Efficient OLEDs: Materials Based on Thermally Activated Delayed Fluorescence*, Wiley VCH **2018**.
[3] G. Hong, X. Gan, C. Leonhardt, Z. Zhang, J. Seibert, J. M. Busch, S. Bräse, *Adv. Mater.* **2021**, *33*, 2005630.
[4] D. Di, A. S. Romanov, L. Yang, J. M. Richter, J. P. H. Rivett, S. Jones, T. H. Thomas, M. Abdi Jalebi, R. H. Friend, M. Linnolahti, M. E. Bochmann, D. Credgington, *Science* **2017**, *356*, 159–163.
[5] R. Hamze, J. L. Peltier, D. Sylvinson, M. Jung, J. Cardenas, R. Haiges, M. Soleilhavoup, R. Jazzar, P. I. Djurovich, G. Bertrand, M. E. Thompson, *Science* **2019**, *363*, 601–606.
[6] R. Hamze, S. Shi, S. C. Kapper, D. S. Muthiah Ravinson, L. Estergreen, M. C. Jung, A. C. Tadle, R. Haiges, P. I. Djurovich, J. L. Peltier, R. Jazzar, G. Bertrand, S. E. Bradforth, M. E. Thompson, *J. Am. Chem. Soc.* **2019**, *141*, 8616–8626.
[7] M. Gernert, L. Balles-Wolf, F. Kerner, U. Müller, A. Schmiedel, M. Holzapfel, C. M. Marian, J. Pflaum, C. Lambert, A. Steffen, *J. Am. Chem. Soc.* **2020**, *142*, 8897–8909.
[8] J. Föller, C. M. Marian, *J. Phys. Chem. Lett.* **2017**, *8*, 5643–5647.
[9] N. Lüdtke, J. Föller, C. M. Marian, *Phys. Chem. Chem. Phys.* **2020**, *22*, 23530–23544.
[10] A. Steffen, B. Hupp, *Comprehensive Coordination Chemistry III*, Vol. 2 (Eds: E. C. Constable, G. Parkin, L. Que Jr), Elsevier: Oxford **2021**; pp 466–502.
[11] V. Wing-Wah Yam, K. Kam-Wing Lo, *Chem. Soc. Rev.* **1999**, *28*, 323–334.
[12] G. Cheng, G. K.-M. So, W.-P. To, Y. Chen, C.-C. Kwok, C. Ma, X. Guan, X. Chang, W.-M. Kwok, C.-M. Che, *Chem. Sci.* **2015**, *6*, 4623–4635.
[13] J. Tang, H.-Y. Yin, J.-L. Zhang, *Inorganic, Organometallic Transition Metal Complexes with Biological Molecules and Living Cells*, (Ed: K. K.-W. Lo) Academic Press **2017**; pp 1–53.
[14] A. Gusev, E. Braga, E. Zamnius, M. Kiskin, M. Kryukova, A. Baryshnikova, B. Minaev, G. Baryshnikov, H. Ågren, W. Linert, *RSC Adv.* **2019**, *9*, 22143–22152.
[15] A. N. Gusev, M. A. Kiskin, E. V. Braga, M. A. Kryukova, G. V. Baryshnikov, N. N. Karaush-Karmazin, V. A. Minaeva, B. F. Minaev, K. Ivaniuk, P. Stakhira, H. Ågren, W. Linert, *ACS Appl. Electron. Mater.* **2021**, *3*, 3436–3444.
[16] R. Diana, B. Panunzi, *Molecules* **2020**, *25*, 4984.
[17] R. Wang, L. Deng, M. Fu, J. Cheng, J. J. Li, *Mater. Chem.* **2012**, *22*, 23454–23460.
[18] Y. Sakai, Y. Sagara, H. Nomura, N. Nakamura, Y. Suzuki, H. Miyazaki, C. Adachi, *Chem. Commun.* **2015**, *51*, 3181–3184.
[19] T. Yu, V. K.-M. Au, D. P.-K. Tsang, M.-Y. Chan, V. W.-W. Yam, *Dalton Trans.* **2015**, *44*, 18983–18992.
[20] K. D. Oyler, F. J. Coughlin, S. Bernhard, *J. Am. Chem. Soc.* **2007**, *129*, 210–217.
[21] I. Y. Chan, W. G. van Dorp, T. J. Schaafsma, J. H. van der Waals, *Mol. Phys.* **1971**, *22*, 753–760.
[22] A. Harriman, *J. Chem. Soc. Faraday Trans. 1* **1980**, *76*, 1978–1985.
[23] M. Pineiro, A. L. Carvalho, M. M. Pereira, A. M. d R Gonsalves, L. G. Arnaut, S. J. Formosinho, *Chem. Eur. J.* **1998**, *4*, 2299–2307.
[24] K. A. Truesdell, G. A. Crosby, *J. Am. Chem. Soc.* **1985**, *107*, 1787–1788.
[25] G. A. Crosby, R. G. Highland, K. A. Truesdell, *Coord. Chem. Rev.* **1985**, *64*, 41–52.
[26] K. J. Jordan, W. F. Wacholtz, G. A. Crosby, *Inorg. Chem.* **1991**, *30*, 4588–4593.
[27] R. G. Highland, G. A. Crosby, *Chem. Phys. Lett.* **1985**, *119*, 454–458.
[28] R. G. Highland, J. G. Brummer, G. A. Crosby, *J. Phys. Chem.* **1986**, *90*, 1593–1598.
[29] A. M. Galin, Y. V. Razskazovsky, M. Y. Mel'nikov, *J. Photochem. Photobiol. A* **1993**, *72*, 35–40.
[30] P. J. Gronlund, J. A. Burt, W. F. Wacholtz, *Inorg. Chim. Acta* **1995**, *234*, 13–18.
[31] O. Mrózek, M. Gernert, A. Belyaev, M. Mitra, L. Janiak, C. M. Marian, A. Steffen, *Chem. Eur. J.* **2022**, *28*, e202201114.
[32] B. Minaev, H. Ågren, *Chem. Phys.* **2005**, *315*, 215–239.
[33] J. A. Burt, G. A. Crosby, *Chem. Phys. Lett.* **1994**, *220*, 493–496.
[34] T. L. Cremers, D. R. Bloomquist, R. D. Willett, G. A. Crosby, *Acta Crystallogr.* **1980**, *B36*, 3097–3099.
[35] S. Scheins, S.-L. Zheng, J. B. Benedict, P. Coppens, *Acta Crystallogr. Sect. B* **2010**, *66*, 366–372.
[36] G. Baryshnikov, B. Minaev, H. Ågren, *Chem. Rev.* **2017**, *117*, 6500–6537.
[37] B. de Souza, G. Farias, F. Neese, R. Izsák, *J. Chem. Theory Comput.* **2019**, *15*, 1896–1904.
[38] T. J. Penfold, E. Gindensperger, C. Daniel, C. M. Marian, *Chem. Rev.* **2018**, *118*, 6975–7025.
[39] C. M. Marian, *Annu. Rev. Phys. Chem.* **2021**, *72*, 617.
[40] Y. Tsuchiya, S. Diesing, F. Bencheikh, Y. Wada, P. L. dos Santos, H. Kaji, E. Zysman-Colman, I. D. W. Samuel, C. Adachi, *J. Phys. Chem. A* **2021**, *125*, 8074–8089.
[41] Y. Wada, K. Shizu, H. Kaji, *J. Phys. Chem. A* **2021**, *125*, 4534–4539.
[42] A. Rodríguez-Serrano, F. Dinkelbach, C. M. Marian, *Phys. Chem. Chem. Phys.* **2021**, *23*, 3668–3678.
[43] S. W. Park, J. H. Yang, H. Choi, Y. M. Rhee, D. Kim, *J. Phys. Chem. A* **2020**, *124*, 10384–10392.
[44] R. Kamiński, M. S. Schmøkel, P. Coppens, *J. Phys. Chem. Lett.* **2010**, *1*, 2349–2353.
[45] M. J. Frisch, G. W. Trucks, H. B. Schlegel, G. E. Scuseria, M. A. Robb, J. R. Cheeseman, G. Scalmani, V. Barone, G. A. Petersson, H. Nakatsuji, et al., *Gaussian 16, Revision A.03.*, Gaussian Inc. Wallingford CT **2016**.
[46] M. Von Arnim, R. Ahlrichs, R. J. Comput, *Chem.* **1998**, *19*, 1746–1757.
[47] C. Lee, W. Yang, R. G. Parr, *Phys. Rev. B* **1988**, *37*, 785–789.
[48] A. D. Becke, *J. Chem. Phys.* **1993**, *98*, 1372–1377.
[49] J. P. Perdew, K. Burke, M. Ernzerhof, *Phys. Rev. Lett.* **1996**, *77*, 3865–3868.
[50] C. Adamo, V. Barone, *J. Chem. Phys.* **1999**, *110*, 6158–6170.
[51] S. Grimme, J. Antony, S. Ehrlich, H. Krieg, *J. Chem. Phys.* **2010**, *132*, 154104.
[52] F. Furche, R. Ahlrichs, *J. Chem. Phys.* **2002**, *117*, 7433–7447.
[53] S. Hirata, M. Head-Gordon, *Chem. Phys. Lett.* **1999**, *314*, 291–299.
[54] A. Schäfer, H. Horn, R. Ahlrichs, *J. Chem. Phys.* **1992**, *97*, 2571–2577.
[55] D. Figgen, G. Rauhut, M. Dolg, H. Stoll, *Chem. Phys.* **2005**, *311*, 227–244.
[56] E. Cancès, B. Mennucci, J. Tomasi, *J. Chem. Phys.* **1997**, *107*, 3032.
[57] B. Mennucci, E. Cancès, J. Tomasi, *J. Phys. Chem. B* **1997**, *101*, 10506.
[58] R. Ahlrichs, M. Bär, M. Häser, H. Horn, C. Kölmel, *Chem. Phys. Lett.* **1989**, *162*, 165–169.
[59] .TURBOMOLE V6.6 2014, a development of University of Karlsruhe and Forschungszentrum Karlsruhe GmbH, 1989–2007, TURBOMOLE GmbH, since 2007; available from http://www.turbomole.com.
[60] S. Grimme, M. Waletzke, *J. Chem. Phys.* **1999**, *111*, 5645–5655.
[61] C. M. Marian, A. Heil, M. Kleinschmidt, *Mol. Sci.* **2019**, *9*, e1394.
[62] A. Heil, M. Kleinschmidt, C. M. Marian, *J. Chem. Phys.* **2018**, *149*, 164106.
[63] M. Kleinschmidt, J. Tatchen, C. M. Marian, *J. Comput. Chem.* **2002**, *23*, 824–833.
[64] M. Kleinschmidt, C. M. Marian, *Chem. Phys.* **2005**, *311*, 71–79.
[65] M. Kleinschmidt, C. van Wüllen, C. M. Marian, *J. Chem. Phys.* **2015**, *142*, 094301.
[66] B. A. Heß, C. M. Marian, U. Wahlgren, O. Gropen, *Chem. Phys. Lett.* **1996**, *251*, 365–371.
[67] AMFI is an atomic spin-orbit integral program written by B. Schimmelpfennig, University of Stockholm, **1996**.
[68] M. Kleinschmidt, J. Tatchen, C. M. Marian, *J. Chem. Phys.* **2006**, *124*, 124101.
[69] M. Etinski, J. Tatchen, C. M. Marian, *J. Chem. Phys.* **2011**, *134*, 154105.
[70] M. Etinski, J. Tatchen, C. M. Marian, *Phys. Chem. Chem. Phys.* **2014**, *16*, 4740–4751.
[71] Deposition Number(s) 2173213 (for **1**) contain(s) the supplementary crystallographic data for this paper. These data are provided free of charge by the joint Cambridge Crystallographic Data Centre and Fachinformationszentrum Karlsruhe Access Structures service.

Manuscript received: May 24, 2022
Revised manuscript received: August 24, 2022
Accepted manuscript online: September 4, 2022
Version of record online: October 5, 2022